Biophysical Journal
Article

Biophysical Society

Lingering Dynamics in Microvascular Blood Flow

Alexander Kihm,[1] Stephan Quint,[1,2] Matthias W. Laschke,[3] Michael D. Menger,[3] Thomas John,[1] Lars Kaestner,[1,4] and Christian Wagner[1,5,*]

[1]Department of Experimental Physics, Saarland University, Saarbruecken, Germany; [2]Cysmic GmbH, Munich, Germany; [3]Institute for Clinical and Experimental Surgery and [4]Theoretical Medicine and Biosciences, Saarland University, Homburg, Germany; and [5]Physics and Materials Science Research Unit, University of Luxembourg, Luxembourg, Luxembourg

ABSTRACT The microvascular networks in the body of vertebrates consist of the smallest vessels such as arterioles, capillaries, and venules. The flow of red blood cells (RBCs) through these networks ensures the gas exchange in as well as the transport of nutrients to the tissues. Any alterations in this blood flow may have severe implications on the health state. Because the vessels in these networks obey dimensions similar to the diameter of RBCs, dynamic effects on the cellular scale play a key role. The steady progression in the numerical modeling of RBCs, even in complex networks, has led to novel findings in the field of hemodynamics, especially concerning the impact and the dynamics of lingering events when a cell meets a branch of the network. However, these results are yet to be matched by a detailed analysis of the lingering experiments in vivo. To quantify this lingering effect in in vivo experiments, this study analyzes branching vessels in the microvasculature of Syrian golden hamsters via intravital microscopy and the use of an implanted dorsal skinfold chamber. It also presents a detailed analysis of these lingering effects of cells at the apex of bifurcating vessels, affecting the temporal distribution of plasmatic zones of blood flow in the branches and even causing a partial blockage in severe cases.

SIGNIFICANCE Microvascular networks are major sites of gas exchange and nutrient transport to the tissues of the body. The vessel dimensions in these networks can be compared to the size of red blood cells (RBCs), and therefore, individual RBCs may alter the flow dynamics drastically. Because several pathological states are linked to the perturbations of the blood flow in the microvasculature, a physical understanding of the impact of individual RBC dynamics is crucial. This study analyzes the lingering phenomenon of RBCs at bifurcating vessels, obeying severe implications on the distribution of subsequent RBCs up to a partial blockage of entire vessel branches. These effects have been well described in silico; however, systematic studies in vivo are lacking.

INTRODUCTION

The steady transport of nutrients to the tissues of the body, as well as the delivery of oxygen, is crucial for the health state of animals and humans. In unicellular living beings, this task can be achieved by pure diffusion. However, active transport is necessary to ensure this exchange in vertebrates. This process is realized by the synergistic action of the heart, blood, and vasculature (1). A key setting is the pressure difference between the aorta and the vena cava (2). In between, the microvasculature is present, consisting of the smallest vessels such as the arterioles, capillaries, and venules. The diameters of these vessels in the microcirculation are in the range of the size of individual red blood cells (RBCs), which highlights the importance of the deformation ability of RBCs. Because of the overall length of the microvasculature and the cross sections of the vessels present, it is responsible for the largest resistance and hence the largest dissipation of energy in the blood flow (3–5). Because the microcirculation is embedded in the tissues and ensures the perfusion of these and the organs, any alteration in blood flow may have severe consequences on the actual health state. Indeed, several pathological states such as Alzheimer's disease are linked to the disturbance in the microcirculation (6,7). Angiogenesis and angioadaptation are therefore prone to fulfill the metabolic needs of the respective organs and tissues (8,9). The observed architectures range from tree-like networks to mesh-like networks, in which the subsequent diameters of vessels at bifurcations satisfy, in general, Murray's law, although deviations are well

Submitted August 26, 2020, and accepted for publication December 14, 2020.

*Correspondence: c.wagner@uni-saarland.de

Editor: Ana-Suncana Smith.

https://doi.org/10.1016/j.bpj.2020.12.012

known (10,11). Compared with macrovascular blood flow, effects arising from the particulate nature of blood are more pronounced in the microcirculation. Considering the volume fraction of RBCs in whole-blood suspensions, the so-called hematocrit, a temporal heterogeneity, is given in the capillary vessels contrasting a temporal homogeneity ubiquitous in large vessels such as arteries (see Videos S1 and S2). Similarly, the vessel diameter in which the blood flows has been found to have an impact on the local hematocrit (12,13). This so-called Fåhræus effect can be explained by the lateral migration of RBCs to the vessel centerline, leaving a cell-depleted layer close to the vessel walls. As a result, RBCs obey a higher speed on average in the Poiseuille profile than the bulk speed of the plasma. In the seminal work by Fåhræus and Lindqvist (14), the former effect could be identified as one of the major causes of the dependence on the vessel diameter of apparent viscosity in blood solutions. Apart from these observations, phase separation in the microvasculature becomes apparent, leading to a nonhomogeneous distribution of RBCs within the vessels. This phase separation is partially caused by the Fåhræus effect, especially in conjunction with bifurcations, although it is not the only origin. The entirety of the described effects, highlighting the significant impact of the biphasic composition of blood, also shows the necessity of modeling blood in this way.

Recent advances in the modeling of the microvasculature in mammals have led to findings of the dynamics of RBCs, as well as other cellular components, in silico. The complexity of the networks in these studies ranges from one symmetrical bifurcation (15,16) to the mimicking of an anatomically accurate in vivo network consisting of an interconnected mesh-like structure with various branches, confluences, and bifurcations (17–20). In (20), such complex networks have been investigated on a scale that both allows for dense suspensions of RBCs as well as yielding discrete data points of every single RBC, including their individual shape. As a result, deformation and dynamic characteristics of RBCs in the vicinity of bifurcations have been studied, leading to the observation of the so-called lingering events. This phenomenon of RBCs resting at the apex of bifurcations is well known in physiology; however, to our knowledge, no systematic studies have been carried out to address this phenomenon. Further, the results found in (20) are still unmatched by any means in vivo. Thus, this study aims to elucidate the fundamental dynamics of these lingering events in vivo. By means of intravital fluorescence microscopy, it can extract position data out of flowing RBCs in the microcirculatory system of hamsters. Additionally, we have developed algorithms that allow to separate the effect of lingering on the flow of subsequent RBCs. Specifically, we use this approach to show the impact of lingering on the void duration, i.e., cell-deprived zones in the bloodstream.

MATERIALS AND METHODS

Permissions

All the conducted experiments were approved by the local government animal protection committee (permission number: 25/2018) and were performed in accordance with the German legislation on the protection of animals and the National Institutes of Health Guidelines for the Care and Use of Laboratory Animals.

Animal preparation

We briefly describe the necessary steps in the preparation protocol (for a more detailed description, see (21)). Syrian golden hamsters (*Mesocricetus auratus*) with a bodyweight of 60–80 g are equipped with a dorsal skinfold chamber consisting of two symmetrical titanium frames with a total weight of ~4 g. For this purpose, the animals are anesthetized, and from their depilated and disinfected back, one layer of skin and subcutis with the panniculus carnosus muscle, as well as the two layers of the retractor muscle, are completely removed within the area of the observation window of the chamber. A total of five hamsters were prepared to neglect any interindividual effects and to observe different phenomena in various geometries.

Experimental setup

For intravital microscopic analyses of the microcirculation, the hamster is anesthetized by an intraperitoneal injection of 100 mg/kg ketamine and 10 mg/kg xylazine, and 0.1 mL of the blood plasma marker 5% fluorescein-isothiocyanate (FITC)-labeled dextran (150 kDa; Sigma-Aldrich, Taufkirchen, Germany) is injected into the retrobulbar venous plexus for contrast enhancement. Subsequently, the animal is fixed on a stage, allowing for horizontal positioning of the desired field of view under the objective of an upright microscope (Zeiss, Oberkochen, Germany), as previously described for mice (22). Because of the geometry of the observation window (circular with a diameter of 10 mm) and the attached snap ring of the chamber, the use of liquid immersion objectives is provided. To maximize the observation area, one ideally uses narrow objectives because the objective may collide with the frame by examining an area close to the boundaries of the observation window.

In this study, two different objectives are used: a water immersion objective for investigations of capillary blood flow with a magnification of 63× and an air objective with a magnification of 50× (both Zeiss). Its high magnification allows for tracking and analyzing individual RBCs (e.g., the cell shape evolution while passing through confluences or bifurcations). On the contrary, an air objective with increased working distance is used to record blood flow in vessel geometries of bigger dimensions (enlarged field of view) or embedded in deeper tissue layers. The recorded image series consist of up to 6000 images, leading to a time coverage of 4–20 s depending on the actual frame rate of the camera (ORCA-Flash4.0 V3; Hamamatsu Photonics K.K., Hamamatsu, Japan).

Image processing

Because of the inherent properties of a dynamical system, the amount of fluorescent dye in the field of view is highly time dependent. This fact results in a flickering motion in the original footage. Histogram matching has been applied for uniform white balance throughout the images and to suppress these flickering events. A Gaussian blur was then applied to despeckle the images before applying a binary mask to disregard the background and enhance the contrast of the image series. An example of this mask is depicted in Fig. 2, in which the original in vivo geometry can be found along with the corresponding mask, created by averaging all images and tracing the resulting mean image. Particle tracking has been carried out via a custom-tailored MATLAB (The MathWorks, Natick, MA) script (see also

(16,23)). By this technique, we were able to extract the position data of the moving cells. We stress that because of abundant breathing movements, not all images of a series can be analyzed, but rather are split into subseries of images in which no displacements of the vessels are visible. However, alterations in tissue thickness may lead to deficiencies in image quality. The same holds for the fact that vessels are winding in a three-dimensional topology, and thus, the focal plane will only capture a certain part of the geometry. Therefore, a complete automatized analysis is complicated and possible in only some peculiar cases. For most analyses, manual adjustments and evaluations must be carried out. Because the plasma in the hamsters is stained with a fluorescent dye, the apparent RBCs obey lower brightness values than cell-free (plasma-rich) areas. From the corresponding temporal brightness distributions, one can therefore define voids and the passing RBCs. For uniform characterization of void durations τ, we binarized the signal with respect to the mean value, i.e., all the signals above the mean will be considered as void. In each branch, the mean passage time or advection time of RBCs is determined and denoted by τ_{RBC}. For a better comparison within a geometry, we seek to achieve a normalized void duration. Therefore, we have divided the calculated void durations by τ_{RBC} in the respective branch to achieve a normalization by the flow rate. These normalized void durations are then sorted in ascending order to obtain the empirical cumulative distribution function. We postulate this empirical cumulative distribution function to be represented by a log-normal distribution function $\mathrm{cdf}(\tau/\tau_{\mathrm{RBC}})$,

$$\mathrm{cdf}\left(\frac{\tau}{\tau_{\mathrm{RBC}}}\right) = \frac{1}{2}\left[1+\mathrm{erf}\left(\frac{\log\left(\frac{\tau}{\tau_{\mathrm{RBC}}}\right)-\widehat{\mu}}{\sqrt{2}\widehat{\sigma}}\right)\right], \qquad (1)$$

with the error function $\mathrm{erf}(\bullet)$ and parameters $\widehat{\mu}$ and $\widehat{\sigma}$. These parameters are estimated based on our data set of void durations τ_i using the maximal likelihood approach, yielding

$$\widehat{\mu} = \frac{1}{N}\sum_{i=1}^{N}\log\left(\frac{\tau_i}{\tau_{\mathrm{RBC}}}\right)$$

and

$$\widehat{\sigma}^2 = \frac{1}{N-1}\sum_{i=1}^{N}\left(\log\left(\frac{\tau_i}{\tau_{\mathrm{RBC}}}\right)-\widehat{\mu}\right)^2. \qquad (2)$$

Probability density distributions of the normalized void durations are given by differentiation of Eq. 1. The postulation of the log-normal distribution of normalized void durations has been verified a posteriori by a Kolmogorov-Smirnov test. For the geometry in Fig. 2, the corresponding cumulative densities of void durations are depicted in Fig. 3.

RESULTS

We analyze bifurcating vessels in the microvascular system of hamsters (arterioles, capillaries, and venules) with varying diameter and bifurcating angles (details are given in the Materials and Methods). A typical scenario of a lingering event is shown in Fig. 1, in which the temporal evolution of a lingering RBC in an arteriolar bifurcation has been recorded.

We analyzed a variety of different geometries and hamster models (see Supporting Materials and Methods). Most of the analyzed geometries exhibit one apex with two branching vessels; however, we have presented here the interesting data of the more complex geometry with four apices and a total of seven branching vessels (see Fig. 2).

Based on the geometry depicted in Fig. 2, we calculate the integrated brightness signal along a line perpendicular to the respective centerline of the vessel.

To take the lingering into account, we further applied a particle-tracking algorithm yielding trajectories of individual RBCs. Out of these tracking data, we can extract detailed knowledge of the RBC speeds. Because a lingering event is defined by an RBC resting at the apex of a bifurcation, we analyzed the velocity data in a small region around the apex of the respective bifurcation. If, in this region, the speed of passing RBCs obeys a severe drop, we call this a lingering event. The lingering duration is quantized as a time interval when $v_{\mathrm{RBC}} < 30$ μm/s (see Video S3). This value is significantly lower than that of typical cell speeds in the microvasculature, which are in the range of $v_{\mathrm{RBC}} = 100$ μm/s. In general, the tracked center of mass of resting RBCs is limited to a precision of 200–300 nm because of illumination changes. Taking into account that each image captures a time interval of ~10 ms, we thus obtain speed fluctuations of RBC of $v_{\mathrm{RBC}} = 20$–30 μm/s for resting RBCs. We want to stress that the cause of this adaptation is exclusively due to the experimental nature and does not contradict a lingering event, as defined in (20).

In general, the combined application of both the analysis of brightness signals and particle tracking is needed because it cannot be guaranteed that the trajectories cover the whole distance that the single RBCs are traveling because of limited image resolution. On the other hand, the sole evaluation of brightness signals along the vessel centerline will not be sufficient to detect lingering events because of the complex dynamics of RBCs at the apex. Thus, we used a combination of both techniques in the sense that we analyzed void durations by evaluating brightness signals. Additionally, we used particle-tracking data to discriminate lingering RBCs from nonlingering ones. If an RBC is lingering at the bifurcation apex, then the preceding void

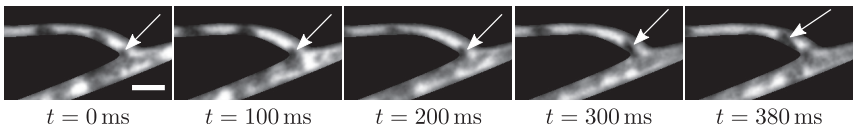

FIGURE 1 Time series of a lingering RBC at an arterial bifurcation for a time interval of $t = 380$ ms. The plasma was fluorescently labeled, and therefore, RBCs appear as dark spots. At $t = 0$ ms, an RBC is touching the apex of the bifurcation, marked by the arrow. The cell starts to deform and linger around this apex, leading to a partial blockage with decreased flow rate, as can be seen in the upper daughter vessel for all subsequent images. Finally, the cell is detached from the apex at $t = 380$ ms. The scale bar represents 10 μm in width. Additional data are provided in Fig. S2.

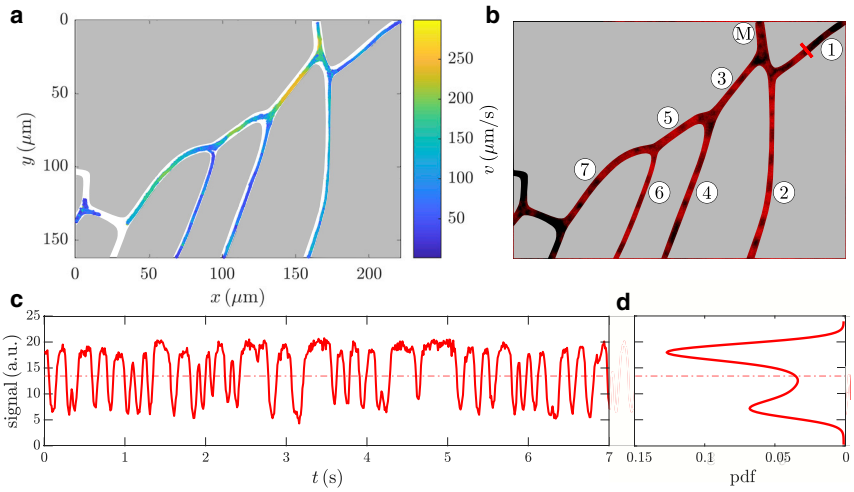

FIGURE 2 (*a*) Results of particle tracking of RBCs in the given geometry. The flow is coming from top (mother vessel "M" in *b*) and exits in all other branches. The color bar corresponds to the tracked speeds, and depicted is the superposition of 500 tracks. (*b*) Snapshot of the geometry with flowing RBCs (*red*) is given. To enhance the contrast and visibility, false color images are shown. The daughter branches are labeled in ascending order from rightmost to leftmost and will be referred to in the main text. (*c*) Distribution of voids within a branch (1) of a bifurcation is shown. The graph corresponds to the measured integrated intensity along a perpendicular line segment with respect to the centerline of this branch (*red line segment* in branch (1) in *b*). Values above the mean value (*red dash-dotted line*) can be regarded as voids, i.e., an absence of cells, whereas values below the mean value correspond to passing cells. On average, voids have a duration of approx. 100 ms; however, because of partial blockage caused by lingering RBCs, void formation can exceed multiple times the average duration, as can be seen at $t \approx 4.7$s, at which a void with a duration of 350 ms is formed. (*d*) Probability density function of the signal intensities from (*c*) is shown with according mean value (*red dash-dotted line*). Because of the pronounced bimodal distribution of signal intensities, the mean value serves as a robust threshold for determining voids from RBCs. The ordinate is identical to the one in (*c*). To see this figure in color, go online.

downstream will be associated with this lingering event. Because of experimental restrictions, we have to deal with not all visible parts of a given vessel being situated in the focal plane because they are exploiting a three-dimensional topology. To overcome this drawback, we obtained the previously described cumulative brightness signal at a vessel segment that is in focus and thus corrected for the spatiotemporal shift of lingering RBCs at the bifurcation apex and the influence on the flow field thereof at a position further downstream. This shift is computed by the average flow speed in the vessel segment. As a result, the impact of distinct lingering scenarios can be associated with the formation of voids at a given position in the daughter branches.

Using the maximal likelihood approach, we estimated the parameters of our empirical distribution, cf. Materials and Methods. In Fig. 3, the good agreement between the data set and the estimated cumulative distribution function is shown. The corresponding probability density functions of voids for the geometry in Fig. 2 are given in Figs. 4 and 5, respectively.

In the first case, only void durations associated with non-lingering events were taken into account, whereas void durations exclusively associated with lingering events were taken into account in the latter case. By comparing the graphs for each branch in both the figures, the influence of lingering on the void durations is obvious. In Fig. 4, the median values of the empirical probability distribution for all graphs are narrowly distributed. In contrast with this state, for voids associated with lingering events (Fig. 5), we find a shift of medians toward higher void durations. A severe case of this observation can also be seen in the inset graph of Fig. 5, in which the median void duration was more than double in the lingering case with respect to non-lingering events.

In addition to the probability densities of void durations, we can also define a so-called lingering frequency as the fraction of voids not associated with lingering events and the total number of occurring voids in a branch of the network. Fig. 6 shows the calculated lingering frequencies of all the analyzed vessels in relation to the normalized mean flow rate in the respective vessel. The normalization factor is given by the mean flow rate of the mother or feeding vessel, which is equal to the sum of the flow rates of all draining vessels due to the incompressibility of the fluid. Even though the size of RBCs is comparable to the apparent vessel diameters, their speed may serve as a good approximation of the mean speed of the surrounding fluid (plug flow); hence, we find

$$Q = \Delta V/\Delta t = A\, v_{\text{fluid}} \simeq A\, l_{\text{RBC}}/\tau_{\text{RBC}}, \tag{3}$$

with the time-averaged flow rate Q, the volume element ΔV, the cross-sectional area A, mean speed of the fluid v_{fluid}, the length of the major axis of the circumscribing ellipse of RBCs l_{RBC}, and the average cell passage time τ_{RBC}, as introduced in previous paragraphs. Among all the investigated pairs of bifurcating vessels, we find the lingering frequency to be higher in the one with lower flow rates with respect to its counterpart with a higher flow rate.

So far, the void durations have been analyzed to elucidate the effect of lingering on the distribution of flowing RBCs upstream the bifurcation apex. A more intuitive observable in the context of hemodynamics is the tube hematocrit H_{T}, and a mapping between these two observables can be derived based on Eq. 3 as

$$H_{\text{T}} = \frac{V_{\text{RBC}}}{V_{\text{RBC}} + V_{\text{void}}} \simeq \frac{1}{1 + \frac{\tau}{\tau_{\text{RBC}}}}, \tag{4}$$

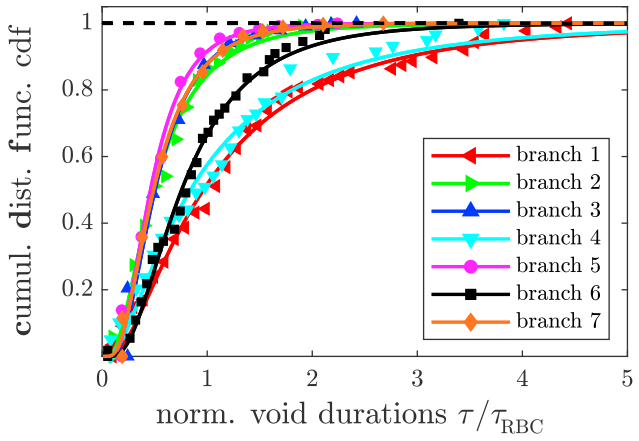

FIGURE 3 Cumulative distribution functions of void durations τ for all branches of the geometry in Fig. 2. The temporal length of the voids is hereby scaled for each branch by the average time of a RBC to pass, τ_{RBC}. The data points correspond to measured void durations, whereas the solid line corresponds to the respective log-normal distributions with estimated parameters $\widehat{\mu}$ and $\widehat{\sigma}$, as in Eq. 1. To see this figure in color, go online.

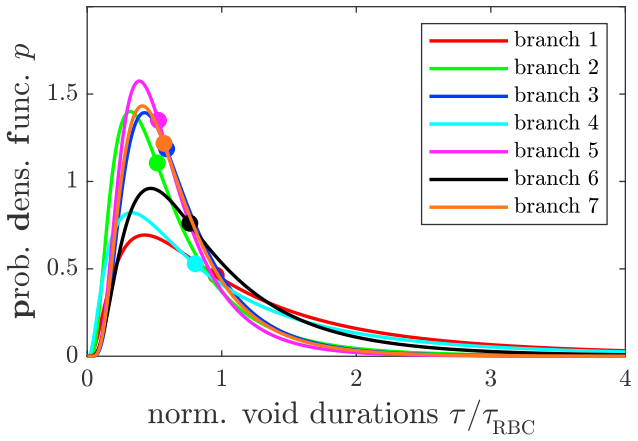

FIGURE 4 Probability density functions of void durations for all branches as in Fig. 3 in the case of nonlingering events. The temporal length of the voids is hereby scaled for each branch by the average time of a RBC to pass, τ_{RBC}. Median values obtained from estimated parameters in Eq. 2 are indicated by solid circles in the respective color code. To see this figure in color, go online.

with the volume fractions V_{RBC} of RBCs and V_{void} of voids, respectively. Besides the intuitive perception of a mesoscopic hematocrit, we favor a truly microscopic observable such as the void durations because crucial information of interspatial distance is easily accessible by the void distributions yet missing in the hematocrit picture.

Apart from lingering at bifurcations, RBCs may also deform in the vicinity of branches, i.e., bifurcations or confluences. Although lingering implies the strong interaction of the vessel walls, the sole presence of junctions may induce shape changes for approaching or distancing RBCs. The main difference is the reduction of the speed, which is significant in the case of lingering but adapted to the flow rates in the respective branch in the latter case, although slight deviations may occur. To analyze the spatiotemporal evolution of this deformation, we calculated the circumscribing ellipse for each individual RBC for all consecutive images, yielding both the centroid position as well as the eccentricity of the cell, given as the ratio of the distance between the two foci and the length of its major axis. Fig. 7 shows the measured eccentricity values for the flowing RBCs in the confluence-bifurcation geometry, both individually as well as the average curve (see Video S4). The corresponding geometry exhibiting both a bifurcation and a confluence is shown as an inset of Fig. 7. From the average curve, one can clearly see the transition of cell shapes RBCs undergo while flowing. At the position of the confluence apex x_{c}, the mean eccentricity exhibits the global minimum, implying the roundest obtained shape. Similarly, at the position of the bifurcation apex x_{b}, the mean eccentricity exhibits a local minimum, indicating a transformation from an elongated to a more spherical shape when approaching the apex and again elongating when entering one daughter branch.

DISCUSSION

Because we analyzed the void formation downstream in a bifurcating vessel geometry, the apparent increase in median void durations originates from two possible scenarios. One contribution is given by the redistribution of consecutive RBCs into the adjacent daughter vessel. The second contribution is given by a change in void speed due to an altered flow rate in the vessel that has an impact on the temporal void duration. In the latter case, the spatial distance between the consecutive RBCs would be sustained, outmatching the observed state. Indeed, by considering the standard deviation of the speeds of passing RBCs in a vessel, variations of the flow rates are negligible. Thus, temporal void durations and spatial void lengths are highly correlated, and this implies a breakup of clusters of RBCs approaching a bifurcation apex. The term cluster hereby implies the state of RBCs moving in a chain in which the intercellular distance is on the order of the cellular size, where hydrodynamic interactions are abundant (24,25). However, we emphasize that the increase of the median void durations in the case of lingering RBCs does not hold for all the analyzed geometries (see Supporting Materials and Methods).

Cases not showing the reported median increase of lingering associated voids can be explained regarding the heterogeneity of RBCs in the overall blood flow within the microvasculature. When cellular effects become more pronounced as the vascular dimensions decrease, the heterogeneity of the blood flow increases. One of the effects associated with this increase in heterogeneity is the Zweifach-Fung effect, leading to a disproportionate partitioning of cells at a bifurcation (26,27). Subsequently, the distribution of RBCs, and thus voids, is highly heterogeneous, as the irregular distributions of RBCs in a feeding vessel are then

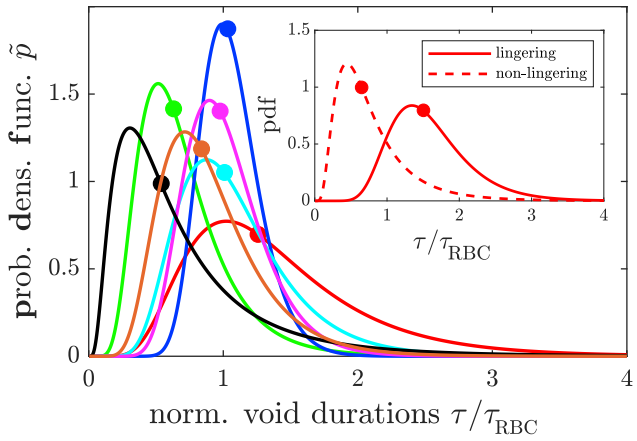

FIGURE 5 Probability density functions of scaled void durations for all branches if only lingering events are taken into account. We define a lingering event to occur if the speed of an RBC is lower than $v_{\mathrm{RBC}} \leq 30$ μm/s in the vicinity of a bifurcation apex. The legend is identical to the one in Fig. 3. The inset graph refers to the geometry depicted in Fig. 1 and shows both the probability densities in the case of lingering and nonlingering, respectively to represent extreme cases of the median shift. Additional information about this geometry can also be found in Fig. S2. Filled circles in matching colors denote median values of normalized void durations, obtained from estimated parameters in Eq. 2. To see this figure in color, go online.

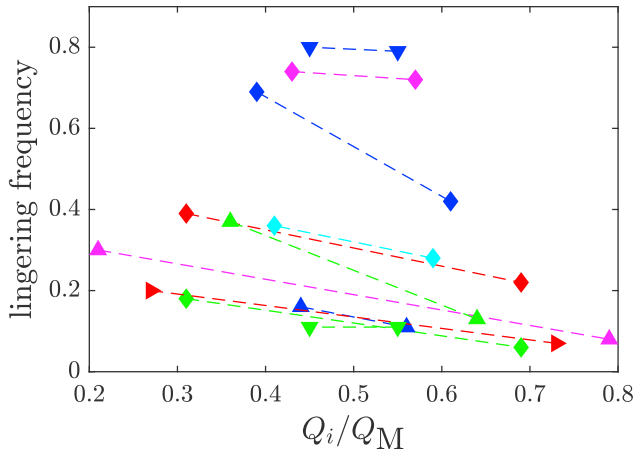

FIGURE 6 Lingering frequencies of the detected voids in relation to the normalized mean flow rate in a distinct vessel. The lingering frequency is hereby defined as the fraction of the void count associated with a lingering event and the total void count in the vessel. Further, we define the normalized mean flow rate as a fraction of the flow rate in a daughter vessel Q_i and the mother vessel Q_{M}. Identical color codes belong to pairs of vessels branching from the same apex; the dashed lines connect the data points of vessels. The unique identifiers for the data points of the lingering frequency are blue for branches (1) and (2), green for branches (4) and (5), and pink for branches (6) and (7), respectively. To see this figure in color, go online.

subdivided into irregular distributions in the daughter vessels. These heterogeneous distributions of cells and voids, respectively, are mirrored in our data, and this heterogeneity manifests in the long tails in the probability density functions. Yet, because lingering events are always caused by the presence of RBCs, the median durations for those lingering associated voids are then decreased with respect to the nonlingering associated voids.

Further, we also notice a suppression of very short void durations, as can be seen from the comparison of Figs. 4 and 5. To quantify this statement, we calculated the probabilities for void durations being less than 0.5 τ_{RBC}. In the case of nonlingering, integration of the corresponding probability densities yields for the probabilities $P_i(\tau_{\mathrm{void}} < 0.5\ \tau_{\mathrm{RBC}}) = \{0.23, 0.47, 0.38, 0.31, 0.45, 0.27, 0.40\}$, $i \in \{1, \ldots, 7\}$, where i denotes the branch identifier according to Fig. 2. Similarly, we obtain $\tilde{P}_i(\tau_{\mathrm{void}} < 0.5\ \tau_{\mathrm{RBC}}) = \{0.02, 0.30, 0.00, 0.03, 0.01, 0.46, 0.10\}$, $i \in \{1, \ldots, 7\}$, with the probabilities $\tilde{P}_i$ in the case of lingering. If one compares these values for each branch, it is obvious that void durations less than or equal to 0.5 τ_{RBC} are suppressed drastically in all but $i = 6$.

In some of the graphs showing the probability densities of the void durations, rather long-tailed distributions are present. We stress that these tails arise inherently because of the heterogeneous distribution of RBCs in the microvascular networks, leading to cell-depleted sequences in branches and thus long void durations in absence of lingering cells.

One crucial question is the dependence of the lingering frequency on the flow properties. Fig. 6 indicates a decreased frequency for the branch with the higher flow rate with respect to the adjacent vessel.

This correlation is coincident with predictions from the Zweifach-Fung effect (26), stating that of adjacent bifurcating vessels, the one with the higher flow rate is entered by relatively more RBCs than its counterpart. The latter vessel thus obeys a decreased hematocrit. The underlying principle of this phenomenon, however, is based on the statistical partitioning involving a skewed force balance of particles at the apex. Yet, an intricate interaction of the RBC when attached to the apex is not considered. The "classical" RBC partitioning is therefore underestimating the disproportionate hematocrit partitioning. We rather assume that because of the increased void durations for lingering associated voids, in conjunction with the increased lingering frequency, the hematocrit in the branch obeying the lower flow rate is even further decreased because of the lingering effect. Qualitatively, these findings match the underprediction of the classical cell partitioning in silico (28), in which the finite sizes of RBCs and interactions with both the endothelium and other RBCs are identified as a main cause for this result. Recent investigations on bifurcating blood flow in vitro indicate a strong dependence of the RBC partitioning on cell deformability and hematocrit (29,30). Currently, in vitro experiments on a scale ≤ 10 μm addressing network effects are rare because of the complexity of the fabrication procedure. Nonetheless, there has been significant progress in mimicking realistic microvascular networks in vitro and addressing partitioning of RBCs in subsequent bifurcations (31) and dilating vessels (32,33). Albeit most results from

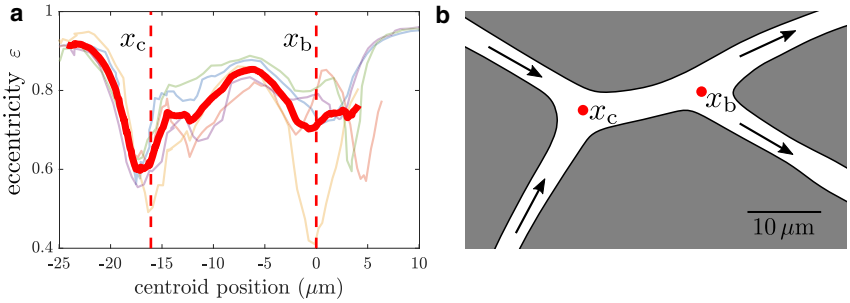

FIGURE 7 Eccentricity ε of RBCs as a function of the centroid position within the geometry shown as the inset. The eccentricity is hereby calculated as the ratio of the distance between the two foci and the length of its major axis of an ellipse with identical second moments for each individual RBC for all consecutive images. The thick red solid line represents the average of all individual graphs (*thin lines*). For the analysis, only single RBCs are considered, whereas trains of flowing RBCs are neglected. The offset of the centroid position is chosen in a way that the bifurcation apex x_b is at position zero. To see this figure in color, go online.

these in vitro experiments show a good to very good agreement with the corresponding outcome in silico, the lingering of cells at bifurcations remain rare events in vitro, and therefore, no systematic studies exist with a focus on this topic. We attribute this scarcity of lingering phenomena in vitro to the fact that bifurcation apices are typically less smooth in artificial networks than in their counterparts in vivo and to the complex interaction of cellular compounds with the endothelial walls of the vessels (34).

So far, we have focused on the impacts of lingering RBCs on the microvascular blood flow in vivo. However, the physical prerequisites to obey lingering have not been discussed yet. RBCs obey an inner network of spectrin fibers, as they are responsible for their biconcave shape at rest. Because of the flexibility of this spectrin network, RBCs can pass through constrictions much smaller than their size at rest (35,36). Yet not only do constrictions alter the shape of RBCs, but so does the complex structure of the vascular network itself, exhibiting merging and bifurcating vessels. The shape of RBCs undergoes a characteristic deformation when approaching the apex of a bifurcation or a confluence, respectively (cf. Fig. 7). Recently, this behavior was reproduced in silico for a varying number of passing cells (15). Whereas this alteration of the shape is due to increasing or decreasing confinements depending on the geometry, it is responsible for the observed lingering behavior. Particles such as hard spheres obey a less severe coupling with the fluid, and we assume the deformation and the strong fluid-cell interaction of RBCs is the major cause of lingering (37).

CONCLUSIONS

We used cutting-edge intravital microscopy in conjunction with a combined sophisticated signal processing algorithm and particle tracking to obtain detailed information of flowing RBCs in living hamster models. Based on these data, we define and detect so-called lingering events, i.e., RBCs resting at a bifurcation apex of branching vessels. We show that these lingering events particularly cause a redistribution of subsequent RBCs in the adjacent daughter vessels and lead to a breakup of trains of RBCs. We further analyze the ratio of lingering cells and all traversing RBCs, the so-called lingering frequency, which is found to be higher in the branching vessel with the higher flow rate compared to the adjacent vessel. This frequency imbalance can be explained intuitively from the disproportionate partitioning of RBCs at bifurcations, the Zweifach-Fung effect. Together with the median increase of lingering associated void durations, we consequently find a decreased hematocrit in the daughter vessel exhibiting a lower flow rate. All the presented results of our study show a good qualitative agreement with the in silico results in (20), although, in contrast to the well-defined boundary conditions in silico, the major experimental drawback is the limited insight into the whole model system. These limitations are given by a limited field of view and the sheer complexity of the living hamster model and all its parameters. We therefore had to focus on those structures for which both the image quality and the physical properties are suited to be analyzed. Nevertheless, we can assess the impact of lingering RBCs on the flow behavior of subsequent cells in vivo. We can provide evidence to show that these lingering events cause a breakup of trains of RBCs as well as redistribution in the branching vessels. Even though these effects seem to be rather fine grained, the impact on the whole organism may be severe, given the importance of blood flow to the health state.

SUPPORTING MATERIAL

Supporting Material can be found online at https://doi.org/10.1016/j.bpj.2020.12.012.

AUTHOR CONTRIBUTIONS

M.W.L., M.D.M., L.K., and C.W. designed the research. A.K., M.W.L., and S.Q. performed the research. A.K., and T.J. analyzed the data. A.K. and C.W. wrote the manuscript. M.W.L, S.Q., M.D.M., L.K., and T.J. provided feedback and insights.

ACKNOWLEDGMENTS

A.K., T.J., L.K., and C.W. gratefully acknowledge support from the research unit DFG FOR 2688 - Wa1336/12 of the German Research Foundation. M.W.L. and M.D.M. received support from the research unit DFG FOR 2688 - LA2682/9-1 of the German Research Foundation. This work was supported by the European Union's Horizon 2020 research and

innovation programme under the Marie Skłodowska-Curie grant agreement no. 860436, EVIDENCE (S.Q., L.K., and C.W.). C.W., T.J., S.Q., and A.K. kindly acknowledge the support and funding of the "Deutsch-Französische-Hochschule" (DFH) DFDK CDFA-01-14 "Living fluids."

REFERENCES

1. Kaestner, L. 2013. Calcium signalling Approaches and Findings in the Heart and Blood. Springer, Berlin, Germany.
2. Popel, A. S., and P. C. Johnson. 2005. Microcirculation and hemorheology. *Annu. Rev. Fluid Mech.* 37:43–69.
3. Poiseuille, J. L. M. 1830. Recherches sur les causes du mouvement du sang dans les veines. *Journal Hebdomadaire de Médicine 1.* 10:277–295.
4. Pries, A. R., T. W. Secomb, …, P. Gaehtgens. 1994. Resistance to blood flow in microvessels in vivo. *Circ. Res.* 75:904–915.
5. Gould, I. G., P. Tsai, …, A. Linninger. 2017. The capillary bed offers the largest hemodynamic resistance to the cortical blood supply. *J. Cereb. Blood Flow Metab.* 37:52–68.
6. Gutiérrez-Jiménez, E., H. Angleys, …, L. Østergaard. 2018. Disturbances in the control of capillary flow in an aged APP^{swe}/PS1ΔE9 model of Alzheimer's disease. *Neurobiol. Aging.* 62:82–94.
7. de la Torre, J. C., and G. B. Stefano. 2000. Evidence that Alzheimer's disease is a microvascular disorder: the role of constitutive nitric oxide. *Brain Res. Brain Res. Rev.* 34:119–136.
8. Pries, A. R., and T. W. Secomb. 2014. Making microvascular networks work: angiogenesis, remodeling, and pruning. *Physiology (Bethesda).* 29:446–455.
9. Pries, A. R., T. W. Secomb, and P. Gaehtgens. 1995. Design principles of vascular beds. *Circ. Res.* 77:1017–1023.
10. Murray, C. D. 1926. The physiological principle of minimum work. I. The vascular system and the cost of blood volume. *Proc. Nat. Acad. Sci. USA.* 12:207–214.
11. Sherman, T. F. 1981. On connecting large vessels to small. The meaning of Murray's law. *J. Gen. Physiol.* 78:431–453.
12. Fåhraeus, R. 1929. The suspension stability of the blood. *Physiol. Rev.* 9:241–274.
13. Pries, A. R., T. W. Secomb, …, J. F. Gross. 1990. Blood flow in microvascular networks. Experiments and simulation. *Circ. Res.* 67:826–834.
14. Fåhræus, R., and T. Lindqvist. 1931. The viscosity of the blood in narrow capillary tubes. *Am. J. Physiol.* 96:562–568.
15. Ye, T., and L. Peng. 2019. Motion, deformation, and aggregation of multiple red blood cells in three-dimensional microvessel bifurcations. *Phys. Fluids.* 31:021903.
16. Bächer, C., A. Kihm, …, S. Gekle. 2018. Antimargination of microparticles and platelets in the vicinity of branching vessels. *Biophys. J.* 115:411–425.
17. Pozrikidis, C. 2009. Numerical simulation of blood flow through microvascular capillary networks. *Bull. Math. Biol.* 71:1520–1541.
18. Bagchi, P. 2007. Mesoscale simulation of blood flow in small vessels. *Biophys. J.* 92:1858–1877.
19. Balogh, P., and P. Bagchi. 2017. A computational approach to modeling cellular-scale blood flow in complex geometry. *J. Comput. Phys.* 334:280–307.
20. Balogh, P., and P. Bagchi. 2017. Direct numerical simulation of cellular-scale blood flow in 3D microvascular networks. *Biophys. J.* 113:2815–2826.
21. Laschke, M. W., B. Vollmar, and M. D. Menger. 2011. The dorsal skinfold chamber: window into the dynamic interaction of biomaterials with their surrounding host tissue. *Eur. Cell. Mater.* 22:147–164, discussion 164–167.
22. Hertz, L., S. Ruppenthal, …, L. Kaestner. 2019. The evolution of erythrocytes becoming red in respect to fluorescence. *Front. Physiol.* 10:753.
23. Guckenberger, A., A. Kihm, …, S. Gekle. 2018. Numerical-experimental observation of shape bistability of red blood cells flowing in a microchannel. *Soft Matter.* 14:2032–2043.
24. Clavería, V., O. Aouane, …, C. Wagner. 2016. Clusters of red blood cells in microcapillary flow: hydrodynamic versus macromolecule induced interaction. *Soft Matter.* 12:8235–8245.
25. Brust, M., O. Aouane, …, C. Wagner. 2014. The plasma protein fibrinogen stabilizes clusters of red blood cells in microcapillary flows. *Sci. Rep.* 4:4348.
26. Fung, Y. C. 1973. Stochastic flow in capillary blood vessels. *Microvasc. Res.* 5:34–48.
27. Svanes, K., and B. W. Zweifach. 1968. Variations in small blood vessel hematocrits produced in hypothermic rats by micro-occlusion. *Microvasc. Res.* 1:210–220.
28. Balogh, P., and P. Bagchi. 2018. Analysis of red blood cell partitioning at bifurcations in simulated microvascular networks. *Phys. Fluids.* 30:051902.
29. Shen, Z., G. Coupier, …, T. Podgorski. 2016. Inversion of hematocrit partition at microfluidic bifurcations. *Microvasc. Res.* 105:40–46.
30. Mantegazza, A., F. Clavica, and D. Obrist. 2020. *In vitro* investigations of red blood cell phase separation in a complex microchannel network. *Biomicrofluidics.* 14:014101.
31. Kodama, Y., H. Aoki, …, K. Tsubota. 2019. In vitro analysis of blood flow in a microvascular network with realistic geometry. *J. Biomech.* 88:88–94.
32. Mantegazza, A., M. Ungari, …, D. Obrist. 2020. Local vs. global blood flow modulation in artificial microvascular networks: effects on red blood cell distribution and partitioning. *Front. Physiol.* 11:566273.
33. Clavica, F., A. Homsy, …, D. Obrist. 2016. Red blood cell phase separation in symmetric and asymmetric microchannel networks: effect of capillary dilation and inflow velocity. *Sci. Rep.* 6:36763.
34. Pries, A. R., and T. W. Secomb. 2005. Microvascular blood viscosity in vivo and the endothelial surface layer. *Am. J. Physiol. Heart Circ. Physiol.* 289:H2657–H2664.
35. Mohandas, N., and E. Evans. 1994. Mechanical properties of the red cell membrane in relation to molecular structure and genetic defects. *Annu. Rev. Biophys. Biomol. Struct.* 23:787–818.
36. Heinrich, V., K. Ritchie, …, E. Evans. 2001. Elastic thickness compressibilty of the red cell membrane. *Biophys. J.* 81:1452–1463.
37. Happel, J., and H. Brenner. 1981. Low Reynolds Number Hydrodynamics. Mechanics of Fluids and Transport Processes. Springer, Dordrecht, The Netherlands.

Biophysical Journal, Volume *120*

Supplemental Information

Lingering Dynamics in Microvascular Blood Flow

Alexander Kihm, Stephan Quint, Matthias W. Laschke, Michael D. Menger, Thomas John, Lars Kaestner, and Christian Wagner

Supplementary information to "Lingering dynamics in microvascular blood flow"

A. Kihm, S. Quint, M. W. Laschke, M. D. Menger,
T. John, L. Kaestner, and C. Wagner

This supplementary material is structured as follows: In section S1, an overview of all geometries found in investigated hamster models and the binarized mask of the bifurcating vessel system is shown as well as the probability densities of the corresponding void durations. We emphasize that, although the total recorded dataset comprises more geometries, the shown ones are the only scenarios suitable for application of a single particle tracking due to the image quality. Section S2 is the caption of the corresponding movie being provided as a separate video file. Section S3 is the movie caption of a video illustrating the integrated intensity signal over time. In section S4 the movie caption is given for the video file that illustrates the lingering algorithm for two tracked RBCs in the microvasculature. Section S5 shows the deformation behavior of RBCs approaching an apex. All datasets and algorithms are provided upon request upon the author.

S1 Additional lingering geometries

S1.1 Geometry 1

The presented geometry in Fig. 1 consists of one feeding vessel (M) and two daughter vessels, with vessel (1) being the only one in the focal plane and thus the developed particle tracking algorithm is applicable. As the lingering frequency, n_{linger}, we define the fraction of voids associated with a lingering event and the total number of voids detected in the respective branch. For the given geometry, we find $n_{1,\text{linger}} = 0.13$. Similarly to the technique in the main article we find for the probabilities of void durations less or equal than half the mean passage time of RBCs, $P_1\left(\tau_{\text{void}} < 0.5\,\tau_{\text{RBC}}\right) = 0.44$. By only considering such voids associated with lingering scenarios, we find for the corresponding probabilities $\tilde{P}_1\left(\tau_{\text{void}} < 0.5\,\tau_{\text{RBC}}\right) = 0.02$. This reflects the observations from the geometry in the main article, where suppression of short void durations due to lingering takes place as well. However, in the case of non-lingering events, larger voids are detected as can be deducted from the tails of the probability density functions. One contribution to these long void durations is the heterogeneous distribution of RBCs in the microvascular system, leading to highly irregular spaced distances between RBCs. The diameter of the vessel is measured as $d_1 = 2.9\,\mu$m at the position of intensity measurements. Due to experimental restrictions, neither the flowrate in the mother vessel can be obtained nor the flowrate in the second draining vessel, and thus, we cannot provide a normalized flowrate of vessel (1).

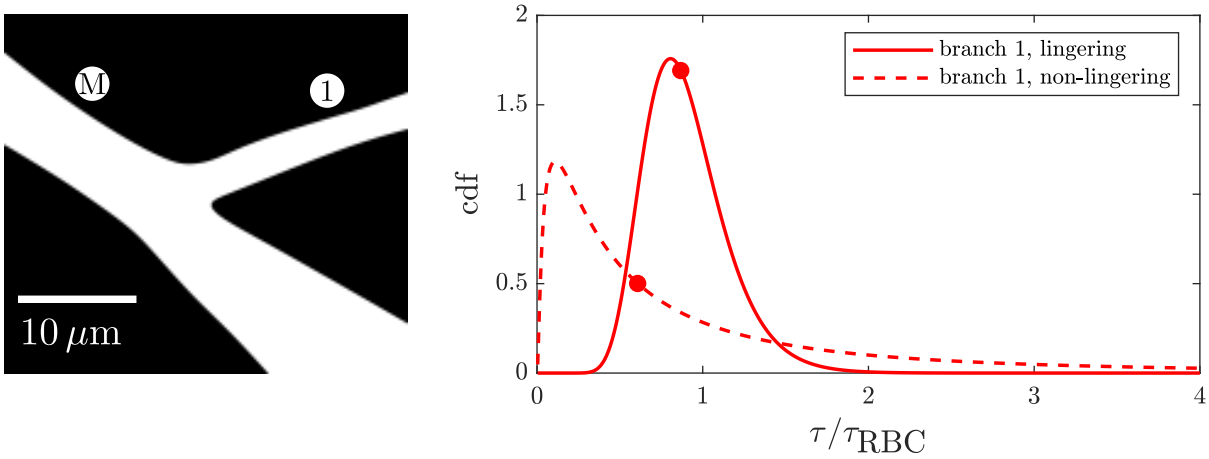

Figure 1: (left) Binary mask (evaluated manually), according to the geometry in vivo. The flow is coming from the mother vessel (M) and exits in the two daughter branches. (right) Normalized void durations associated with non-lingering events in vessel (1) (dashed line) and for lingering events (solid line). In both cases, the normalization has been obtained by the mean of all passing RBCs in the respective branch. This normalization corresponds to normalization by the flowrate. Respective median values are marked by filled circles.

S1.2 Geometry 2

Analogously to the analysis conducted in the previous geometry we obtain a lingering frequency of $n_{1,\text{linger}} = 0.83$ whereas the second daughter vessel again is not suitable for analysis in Fig. 2. The calculated probabilities yield $P_1\left(\tau_{\text{void}} < 0.5\,\tau_{\text{RBC}}\right) = 0.33$ and $\tilde{P}_1\left(\tau_{\text{void}} < 0.5\,\tau_{\text{RBC}}\right) = 0.00$, resp. One can see out of the given void durations for both the lingering and the non-lingering case that short void durations are suppressed in the case of lingering due to redistribution of consecutive RBCs and a spatial distancing between consecutive RBCs. The measured diameter of the vessel is $d_1 = 2.8\,\mu$m, evaluated at the position of intensity measurements. As in the previous case, due to experimental restrictions flowrates are not provided.

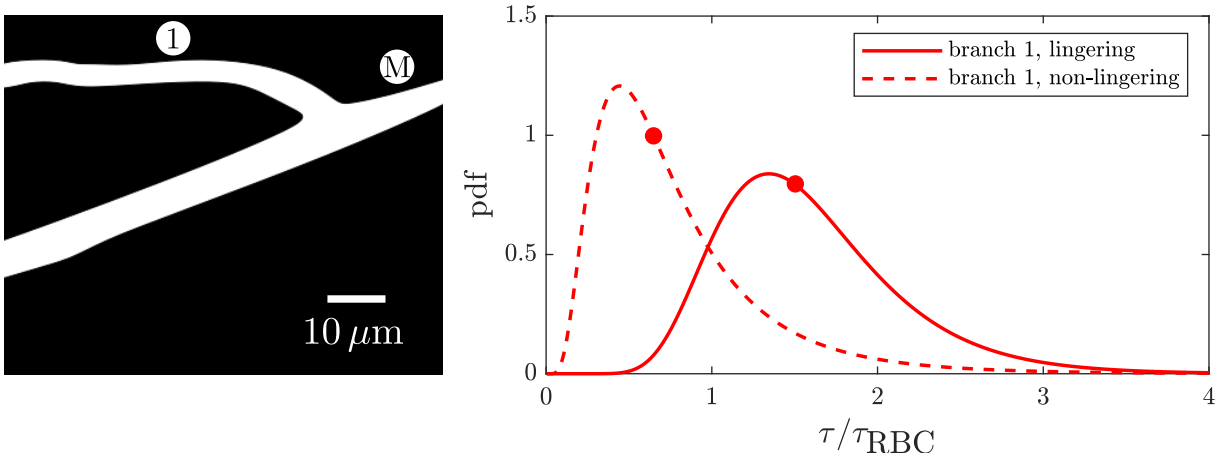

Figure 2: (left) Binary mask (evaluated manually), according to the geometry in vivo. The flow is coming from mother vessel (M) and exits in the two daughter branches. (right) Probability densities of normalized void durations associated to non-lingering events in vessel (1) (dashed line) and for lingering events (solid line). In both cases, the normalization has been obtained by the mean of all passing RBCs in the respective branch. This normalization corresponds to a normalization by the flowrate. We stress that, in the second daughter vessel, RBCs do not travel in a file but rather in a very dense suspension, not allowing for any further analysis on lingering. Respective median values are marked by filled circles.

S1.3 Geometry 3

For the geometry depicted in Fig. 3 we calculate the lingering frequencies as $n_{i,\text{linger}} = \{0.07, 0.20\}$, with $i \in \{1, 2\}$ referring to the vessel identifier. The calculated probabilities yield $P_i\,(\tau_{\text{void}} < 0.5\,\tau_{\text{RBC}}) = \{0.51, 0.22\}$ and $\tilde{P}_i\,(\tau_{\text{void}} < 0.5\,\tau_{\text{RBC}}) = \{0.06, 0.03\}$, resp. Also, the median void duration is increased in the case of lingering events. The vessel diameters yield $d_i = \{4.1, 3.5\}\,\mu$m, with corresponding normalized flowrates $q_i = Q_i/Q_{\text{M}} = \{0.73, 0.27\}$. This geometry is linked to the unique identifier "▸" in Figure 6 of the manuscript.

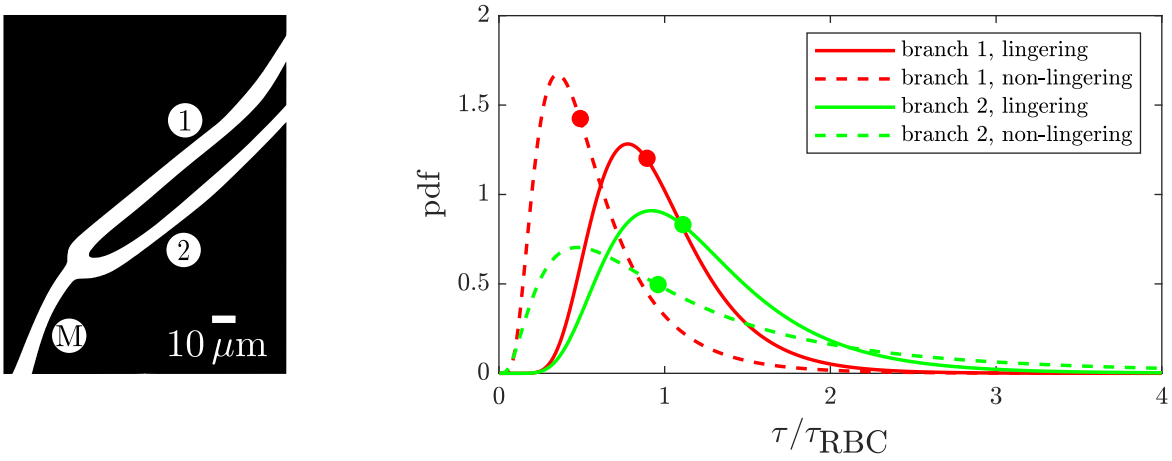

Figure 3: (left) Binary mask (evaluated manually), mimicking the geometry in vivo. The flow is coming from the lower left corner (M) and exits in the two daughter branches as denoted in the sketch. (right) Probability densities of normalized void durations associated to non-lingering events in vessels (1) and (2) (dashed lines) and for lingering events (solid line). In both cases, the normalization has been obtained by the mean of all passing RBCs in the respective branch. Respective median values are marked by filled circles.

S1.4 Geometry 4

The obtained probabilities of void durations τ to be $\tau_{\text{void}} < 0.5\,\tau_{\text{RBC}}$ is given by $P_i\,(\tau_{\text{void}} < 0.5\,\tau_{\text{RBC}}) = \{0.45, 0.59\}$ in the case of non-lingering events and $\tilde{P}_i\,(\tau_{\text{void}} < 0.5\,\tau_{\text{RBC}}) = \{0.37, 0.34\}$ in the case of lingering events, with $i \in \{1, 2\}$ referring to the vessel identifier as depicted in Fig. 4. For the lingering frequencies we find $n_{i,\text{linger}} = \{0.69, 0.42\}$, with the corresponding measured vessel diameters $d_i = \{3.1, 3.6\}\,\mu$m at the position of the signal evaluation. Corresponding average flowrates are determined as $q_i = Q_i/Q_{\text{M}} = \{0.39, 0.61\}$. This geometry is linked to the unique identifier "◆" in Figure 6 of the manuscript.

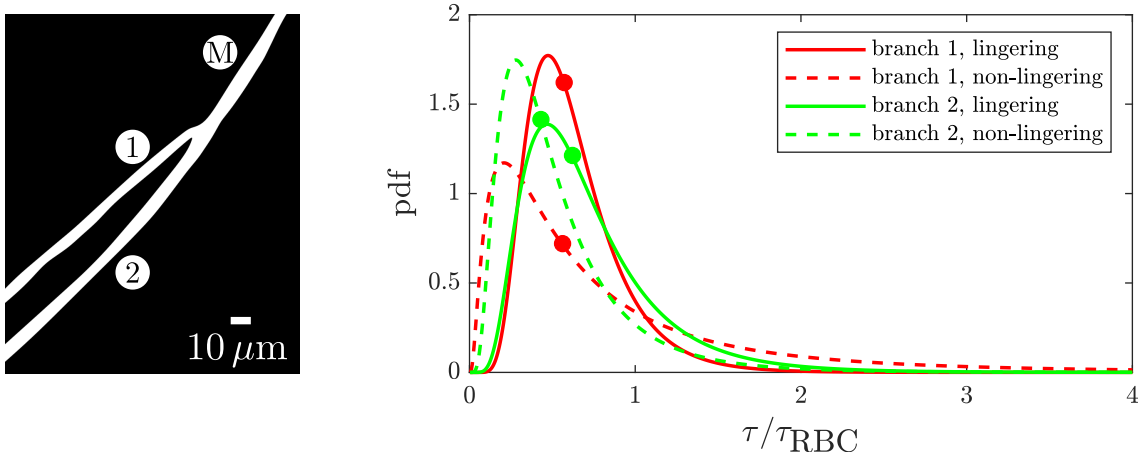

Figure 4: (left) Binary mask (evaluated manually), created according to the geometry in vivo. The flow is coming from the upper right corner (M) and exits in the two daughter branches (1) and (2), resp. as denoted in the scheme. Respective median values are marked by filled circles.

S1.5 Geometry 5

The obtained probabilities of void durations τ to be $\tau_{\text{void}} < 0.5\,\tau_{\text{RBC}}$ is given by $P_i\,(\tau_{\text{void}} < 0.5\,\tau_{\text{RBC}}) = \{0.08, 0.01\}$ in the case of non-lingering events and $\tilde{P}_i\,(\tau_{\text{void}} < 0.5\,\tau_{\text{RBC}}) = \{0.00, 0.00\}$ in the case of lingering events, with $i \in \{1, 2\}$ referring to the vessel identifier as depicted in Fig. 5. For the lingering frequencies we find $n_{i,\text{linger}} = \{0.18, 0.06\}$, with the corresponding measured vessel diameters $d_i = \{3.9, 4.2\}\,\mu$m at the position of the signal evaluation. The mean flowrates yield $q_i = Q_i/Q_{\text{M}} = \{0.31, 0.69\}$. This geometry is linked to the unique identifier "◆" in Figure 6 of the manuscript.

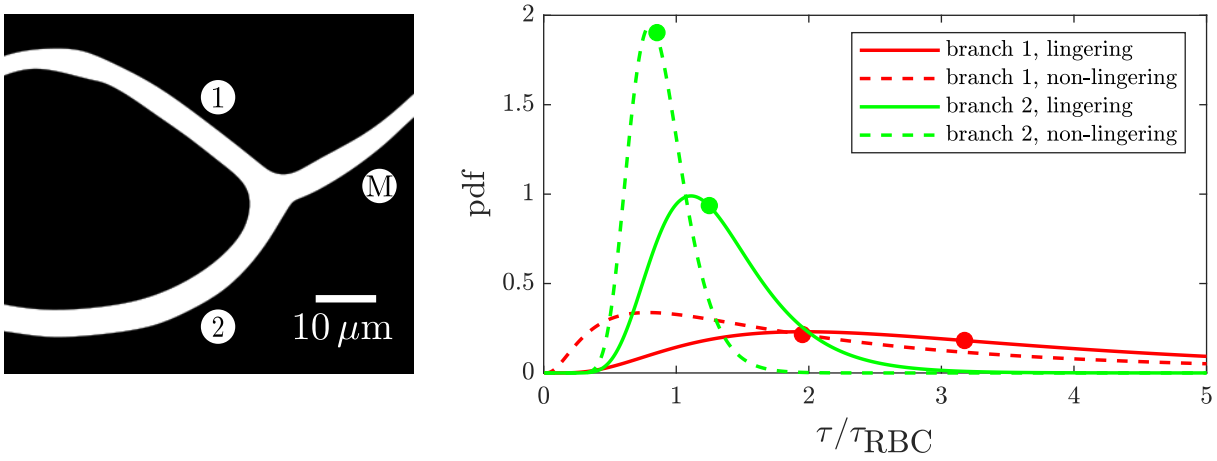

Figure 5: (left) Binary mask (evaluated manually), created according to the geometry in vivo. The flow is coming from the upper right vessel (M) and exits in the two daughter branches (1) and (2), resp. as denoted in the scheme. Respective median values are marked by filled circles.

S1.6 Geometry 6

For the geometry depicted in Fig. 6 we calculate the lingering frequencies as $n_{i,\text{linger}} = \{0.39, 0.22\}$, with $i \in \{1, 2\}$ referring to the vessel identifier. The calculated probabilities yield $P_i\,(\tau_{\text{void}} < 0.5\,\tau_{\text{RBC}}) = \{0.21, 0.41\}$ and $\tilde{P}_i\,(\tau_{\text{void}} < 0.5\,\tau_{\text{RBC}}) = \{0.09, 0.18\}$, resp. Also, the median void duration is increased in the case of lingering events. Vessel diameters yield $d_i = \{2.9, 3.3\}\,\mu$m and we find for the normalized mean flowrates $q_i = Q_i/Q_{\text{M}} = \{0.31, 0.69\}$. This geometry is linked to the unique identifier "◆" in Figure 6 of the manuscript.

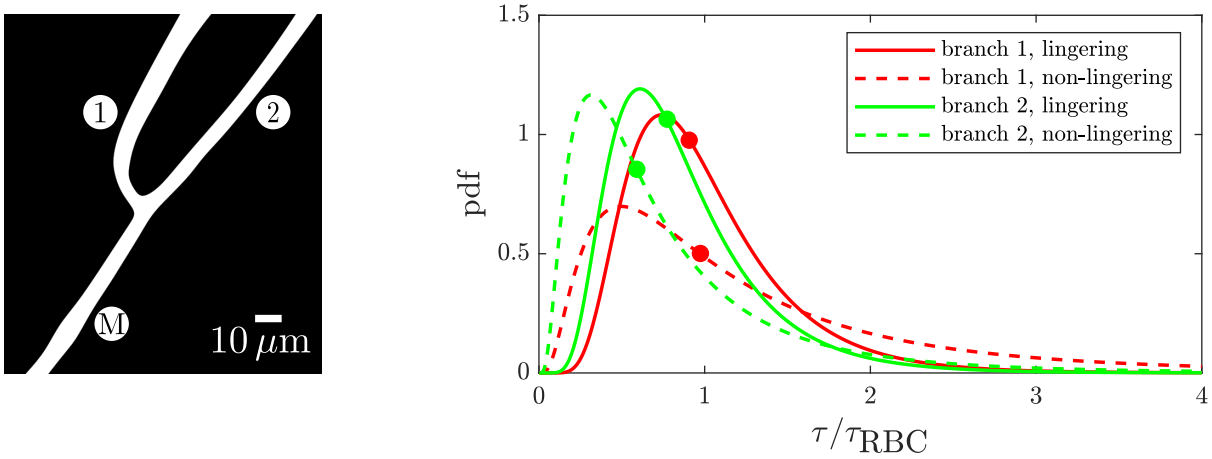

Figure 6: (left) Binary mask (evaluated manually), created according to the geometry in vivo. The flow is coming from the lower left corner (M) and exits in the two daughter branches (1) and (2), resp. as denoted in the scheme. Respective median values are marked by filled circles.

S1.7 Geometry 7

For the geometry depicted in Fig. 7 we calculate the lingering frequencies as $n_{i,\text{linger}} = \{0.28, 0.36\}$, with $i \in \{1, 2\}$ referring to the vessel identifier. The calculated probabilities yield $P_i\,(\tau_{\text{void}} < 0.5\,\tau_{\text{RBC}}) = \{0.55, 0.55\}$ and $\tilde{P}_i\,(\tau_{\text{void}} < 0.5\,\tau_{\text{RBC}}) = \{0.32, 0.49\}$, resp. to find void durations less than half the mean passage time of RBCs. Also, the median void duration is increased in the case of lingering events. We again find the vessel with the smaller diameter obeying a higher lingering frequency compared to the bigger vessel, since the vessel diameters yield $d_i = \{3.1, 2.9\}\,\mu$m, with average normalized flowrates $q_i = Q_i/Q_{\text{M}} = \{0.59, 0.41\}$. This geometry is linked to the unique identifier "🔹" in Figure 6 of the manuscript.

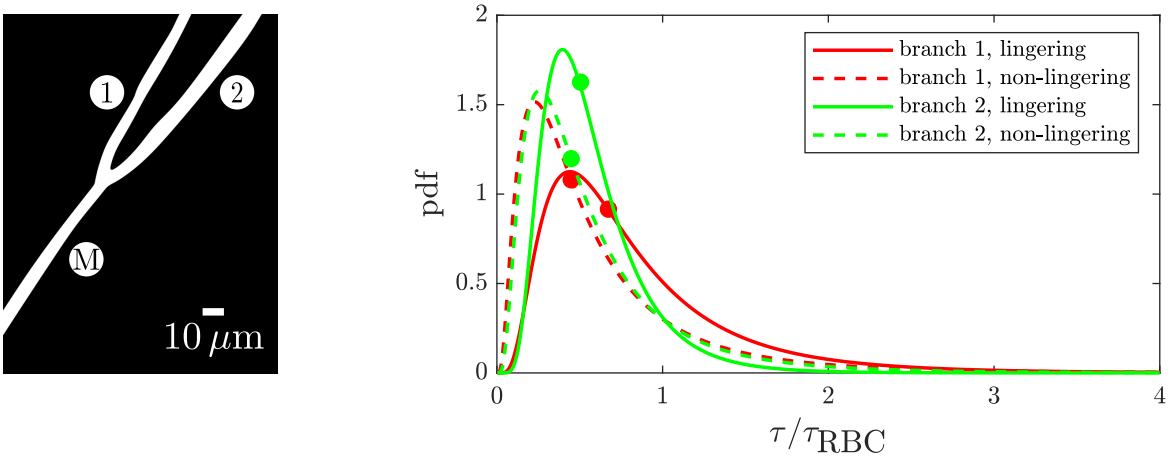

Figure 7: (left) Binary mask (evaluated manually), created according to the geometry in vivo. The flow is coming from the lower left corner (M) and exits in the two daughter branches (1) and (2), resp. as denoted in the scheme. Respective median values are marked by filled circles.

S1.8 Geometry 8

For the geometry depicted in Fig. 8 we calculate the lingering frequencies as $n_{i,\text{linger}} = \{0.74, 0.72\}$, with $i \in \{1, 2\}$ referring to the vessel identifier. The calculated probabilities yield

$P_i\,(\tau_{\text{void}} < 0.5\,\tau_{\text{RBC}}) = \{0.34, 0.34\}$ and $\tilde{P}_i\,(\tau_{\text{void}} < 0.5\,\tau_{\text{RBC}}) = \{0.46, 0.37\}$, resp. to find void durations less than half the mean passage time of RBCs. Although vessel (2) shows similar behavior to the previous results of various geometries, vessel (1) shows opposite behavior. There, the median of void durations not associated to lingering events is increased compared to the lingering case. By further inspection, RBCs travel highly heterogeneous in vessel (1), leading to long RBC depleted zones and thus causing long tails in the probability density distribution of voids. Diameters of both vessels have been determined to $d_i = \{3.3, 2.9\}\,\mu$m and mean flowrates are determined as $q_i = Q_i/Q_{\text{M}} = \{0.43, 0.57\}$. This geometry is linked to the unique identifier "◆" in Figure 6 of the manuscript.

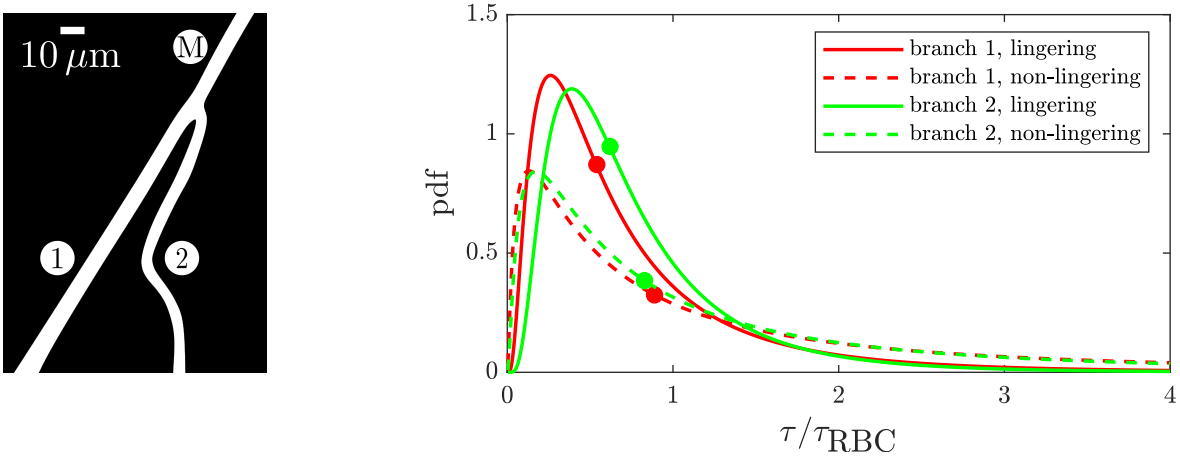

Figure 8: (left) Binary mask (evaluated manually), created according to the geometry in vivo. The flow is coming from the upper right corner (M) and exits in the two daughter branches (1) and (2), resp. as denoted in the scheme. Respective median values are marked by filled circles.

S1.9 Geometry 9

Of all analyzed geometries, the one depicted in 9 is the only one where no lingering events occur (we recall that a lingering event takes place according to the main article, if the velocities of RBCs yield $v_{\text{RBC}} < 30\,\mu$m/s in a circular region around the bifurcation apex. Thus, $n_{i,\text{linger}} = \{0.00, 0.00\}$, $i \in \{1, 2\}$ referring to the vessel identifier. The diameters of the vessels are $d_i = \{2.2, 2.9\}\,\mu$m at the position of the brightness signal evaluation.

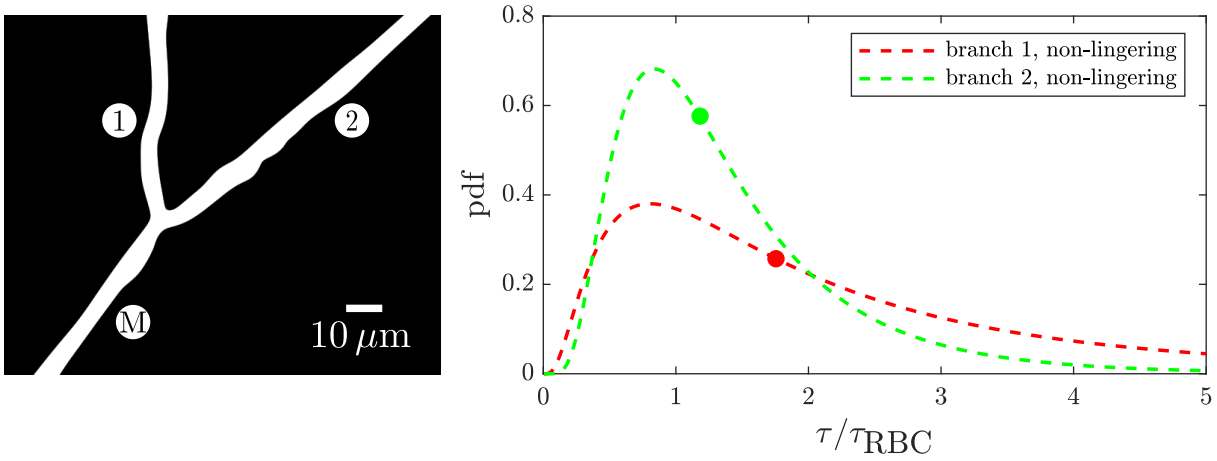

Figure 9: (left) Binary mask (evaluated manually), created according to the geometry in vivo. The flow is coming from the lower left corner (M) and exits in the two daughter branches (1) and (2), resp. as denoted in the scheme. Respective median values are marked by filled circles.

S1.10 Geometry 10

For the geometry depicted in Fig. 10 we calculate the lingering frequencies as $n_{i,\mathrm{linger}} = \{0.79, 0.80\}$, with $i \in \{1, 2\}$ referring to the vessel identifier. The calculated probabilities yield $P_i\,(\tau_{\mathrm{void}} < 0.5\,\tau_{\mathrm{RBC}}) = \{0.29, 0.00\}$ and $\tilde{P}_i\,(\tau_{\mathrm{void}} < 0.5\,\tau_{\mathrm{RBC}}) = \{0.44, 0.44\}$, resp. to find void durations less than half the mean passage time of RBCs. For vessel (1), the peak of the probability density is shifted towards longer void durations in the case of lingering with respect to non-lingering events. However, vessel (2) shows opposite behavior, which we conjecture to be a result of highly heterogeneous RBC distributions entering this branch. We measure equal lingering frequencies, as well as similar mean flowrates in both branches, $q_i = Q_i/Q_{\mathrm{M}} = \{0.55, 0.45\}$. The vessel diameters yield $d_i = \{4.6, 3.4\}\,\mu$m. This geometry is linked to the unique identifier "▼" in Figure 6 of the manuscript.

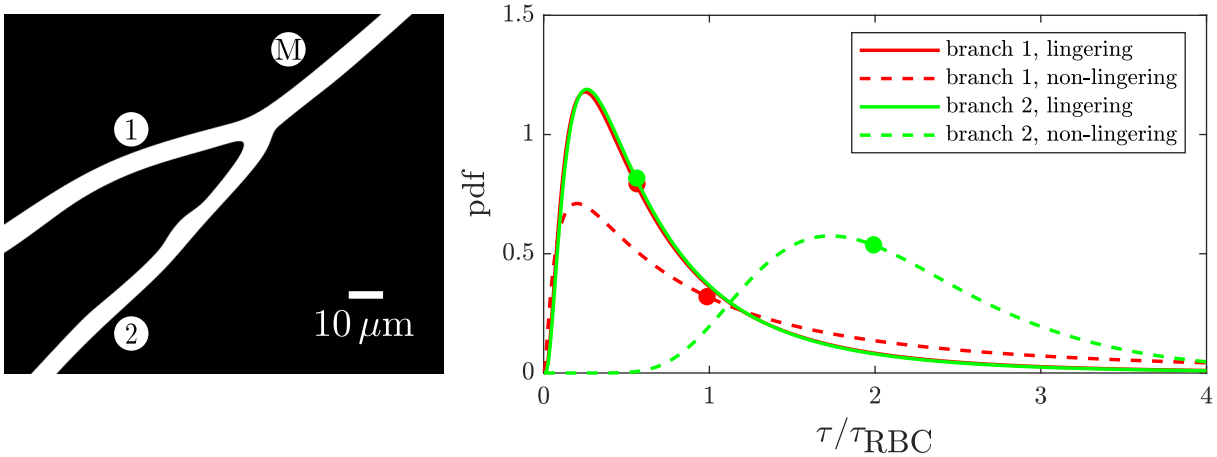

Figure 10: (left) Binary mask (evaluated manually), created according to the geometry in vivo. The flow is coming from the upper right corner (M) and exits in the two daughter branches (1) and (2), resp. as denoted in the scheme. Respective median values are marked by filled circles.

S1.11 Geometry 11

For the geometry depicted in Fig. 11 we calculate the lingering frequencies as $n_{i,\text{linger}} = \{0.44, 0.37\}$, with $i \in \{1, 2\}$ referring to the vessel identifier. The calculated probabilities yield $P_i\,(\tau_{\text{void}} < 0.5\,\tau_{\text{RBC}}) = \{0.21, 0.44\}$ and $\tilde{P}_i\,(\tau_{\text{void}} < 0.5\,\tau_{\text{RBC}}) = \{0.03, 0.19\}$, resp. to find void durations less than half the mean passage time of RBCs. Also, the median void duration is increased in the case of lingering events with respect to non-lingering events. The vessel diameters yield $d_i = \{3.6, 2.8\}\,\mu$m.

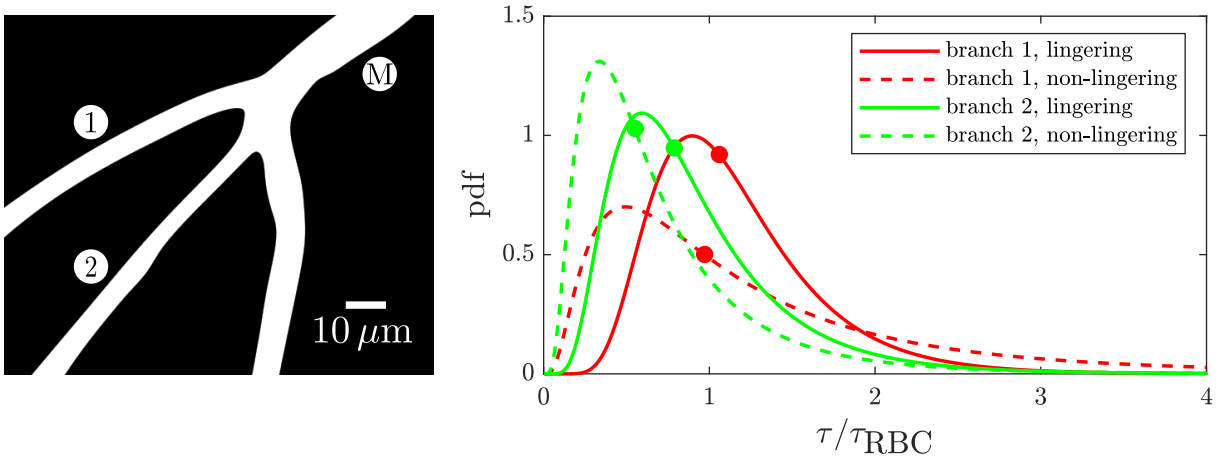

Figure 11: (left) Binary mask (evaluated manually), created according to the geometry in vivo. The flow is coming from the upper right corner (M) and exits in the three daughter branches. However, due to image quality, only vessels (1) and (2), resp. are suited for analysis. Respective median values are marked by filled circles.

S1.12 Geometry 12

For the geometry depicted in Fig. 12 we calculate the lingering frequencies as $n_{i,\text{linger}} = \{0.11, 0.11\}$, with $i \in \{1, 2\}$ referring to the vessel identifier. The calculated probabilities yield $P_i\,(\tau_{\text{void}} < 0.5\,\tau_{\text{RBC}}) = \{0.17, 0.14\}$ and $\tilde{P}_i\,(\tau_{\text{void}} < 0.5\,\tau_{\text{RBC}}) = \{0.04, 0.02\}$, resp. to find void durations less than half the mean passage time of RBCs. Also, the median void duration is increased in the case of lingering events with respect to non-lingering events. The mean flowrates in both branches are fairly similar, $q_i = Q_i/Q_{\text{M}} = \{0.55, 0.45\}$, and again we measure equal lingering frequencies. Vessel diameters are measured as $d_i = \{2.9, 2.3\}\,\mu$m. This geometry is linked to the unique identifier "▼" in Figure 6 of the manuscript.

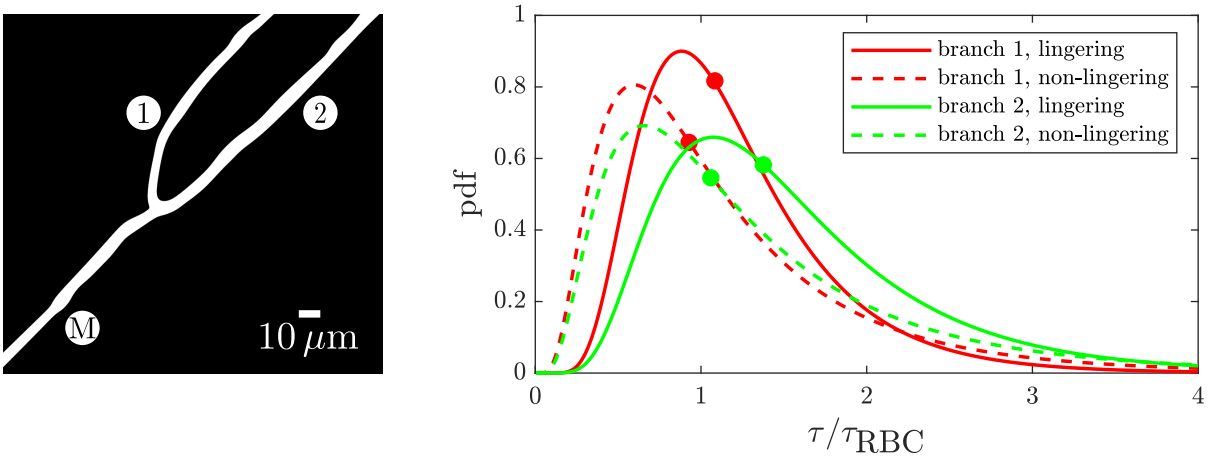

Figure 12: (left) Binary mask (evaluated manually), created according to the geometry in vivo. The flow is coming from the lower left corner (M) and exits in the two daughter branches (1) and (2), resp. as denoted in the scheme. Respective median values are marked by filled circles.

S1.13 Geometry 13

For the geometry depicted in Fig. 13 we calculate the lingering frequency as $n_{1,\text{linger}} = \{0.04\}$. The calculated probabilities yield $P_1\left(\tau_{\text{void}} < 0.5\,\tau_{\text{RBC}}\right) = 0.35$ and $\tilde{P}_1\left(\tau_{\text{void}} < 0.5\,\tau_{\text{RBC}}\right) = 0.01$, resp. to find void durations less than half the mean passage time of RBCs. Also, the median void duration is increased in the case of lingering events with respect to non-lingering events. Due to experimantal restrictions, only vessel (1) can be analyzed properly. The diameter of this vessel is measured to be $d_1 = 2.7\,\mu$m.

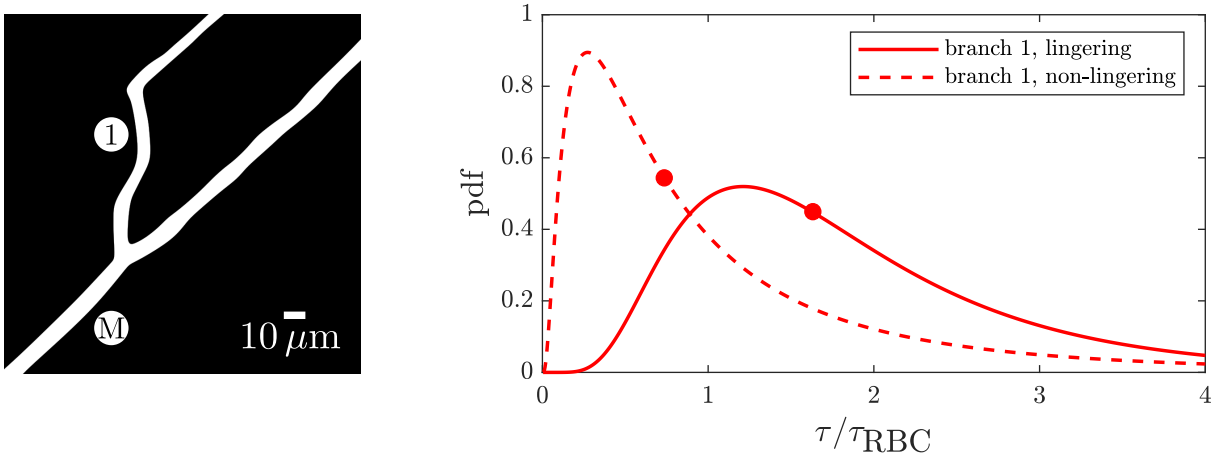

Figure 13: (left) Binary mask (evaluated manually), according to the geometry in vivo. The flow is coming from mother vessel (M) and exits in the two daughter branches. However, due to the focal plane, only vessel (1) is suitable for detecting RBCs. (right) Normalized void durations associated to non-lingering events in vessel (1) (dashed line) and for lingering events (solid line). In both cases, the normalization has been obtained by the mean of all passing RBCs in the respective branch, yielding a normalization by the flowrate. Respective median values are marked by filled circles.

S1.14 Geometry 14

Of all RBCs observed flowing in the case of the geometry depicted in Fig. 14, only 2 showed lingering behavior. Thus the fraction of lingering cells is within the given accuracy vanishing, $n_{1,\text{linger}} = \{0.00\}$, and we also do not show the probability density distribution of two single voids. However, for the sake of completeness we provide the probability densities of voids caused by all non-lingering events. $P_i\,(\tau_{\text{void}} < 0.5\,\tau_{\text{RBC}}) = 0.04$ and the vessel diameter is given as $d_1 = 3.4\,\mu$m.

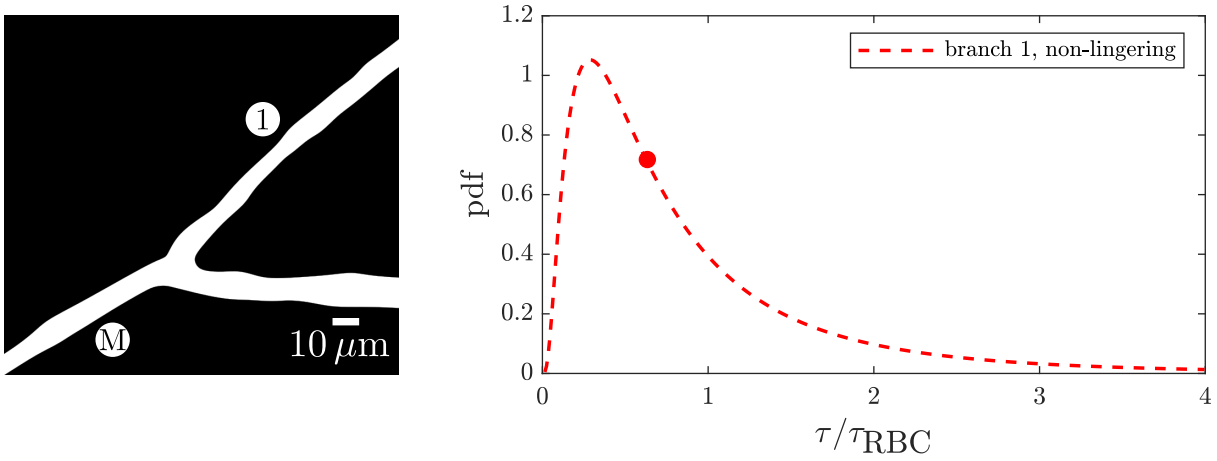

Figure 14: (left) Binary mask (evaluated manually), created according to the geometry in vivo. The flow is coming from the lower left corner (M) and exits in the two daughter branches. Due to image quality, only vessel (1) is suited for analysis. Respective median values are marked by filled circles.

S2 Movie caption

Temporal evolution of microhematocrit evaluated in the red rectangle. The underlying geometry is identical to the one in Fig. 2 in the main manuscript. The highly heterogeneous behavior of the hematocrit value is contrasting the constant hematocrit value found in big vessels, such as e.g. arteries and originates from the particulate nature of blood and resulting heterogeneous distributions of RBCs within the microvascular system.

S3 Movie caption

Intensity signal for the geometry discussed in the main manuscript (cf. Fig. 2 therein). The graph corresponds to the measured cumulative intensity along a perpendicular line segment with respect to the centerline of this branch, indicated by the red line segment in the top part. Values above the mean value can be regarded as voids, i.e. an absence of cells, whereas values below the mean value correspond to passing cells.

S4 Movie caption

Two tracked RBCs with marked centroid positions and circumscribing ellipses. Whereas the RBC marked in red does not exhibit velocities below $v_{\text{RBC}} < 30\mu$m/s at any time and therefore is not considered to show lingering behavior, the cell marked in green does obey velocities below the lingering velocity. Further, the circular region around the bifurcation apex is marked by a red dashed line, in which the velocity has to be less than v_{RBC} for being associated with a lingering

event. The red dashed line in the graph denotes the value of v_{RBC}. For the sake of visibility, we only analyze two RBCs.

S5 Movie caption

According to the geometry depicted in Fig. 7 in the main manuscript we provide a video sequence showing the dynamics of RBCs approaching a bifurcation apex and distancing a confluence apex, resp. Centroid positions of individually flowing RBCs are tracked and marked with dots. In addition, the circumscribing ellipse is shown and the respective eccentricities as a function of centroid position. The playback speed of the video is set to be ($\times$ 0.1) real-time.